Part B

Computational

Contents

I. Statistical Measures **S51**

II. Computational Methods **S52**

III. Method Assessment for Obtaining Molecular Geometries **S56**

IV. Tackling the Conformational Challenge **S57**

IV.I Initial Tests for $[Pd{-}Br{-}Pd]^+$ S57

IV.II Addressing Errors in the SQM PES of $[HBrH{\bullet}2\,OEt_2]^+$ S59

V. Method Assessment for Energy Refinements **S60**

VI. Modeling Isotopic Substitution in the Dynamic K_1 Equilibrium **S62**

VII. List of Abbreviations **S65**

VIII. References **S66**

I. Statistical Measures

The error of a calculated quantitity $q_{\text{calc.}}$ to the experimental reference value $q_{\text{exp.}}$ is given by

$$\Delta q = q_{\text{calc.}} - q_{\text{exp.}} \,. \tag{19}$$

For a set of N errors $\{\Delta q_i\}$, common statistical measures are then defined by the following equations:

$$\text{Mean error: ME} = \frac{1}{N} \sum_{i=1}^{N} \Delta q_i \tag{20}$$

$$\text{Mean absolute error: MAE} = \frac{1}{N} \sum_{i=1}^{N} |\Delta q_i| \tag{21}$$

$$\text{Absolute maximal error: AMAX} = \max_i \left(\{|\Delta q_i|\} \right) \tag{22}$$

$$\text{Maximal error: MAX} = \max_i \left(\{\Delta q_i\} \right) \tag{23}$$

$$\text{Minimal error: MIN} = \min_i \left(\{\Delta q_i\} \right) \tag{24}$$

$$\text{Standard deviation: SD} = \sqrt{\frac{1}{N-1} \sum_{i=1}^{N} \left(\Delta q_i - \text{ME}\right)^2} \tag{25}$$

II. Computational Methods

In general, Gibbs energies of a conformer ensemble (CE) are calculated as

$$G = \overline{G} + G_{\mathrm{conf}} \tag{26}$$

$$= \overline{E}_{\mathrm{gas}} + \overline{\Delta G}_{\mathrm{mRRHO}} + \overline{\Delta G}_{\mathrm{solv}} + G_{\mathrm{conf}}, \tag{27}$$

where all overlined values correspond to Boltzmann-averaged properties[1], which are expensive to compute at higher levels of theory. Hence, G is approximated herein as

$$G \approx E_{\mathrm{gas}} + \Delta G_{\mathrm{mRRHO}} + \Delta G_{\mathrm{solv}} + \underbrace{\overline{G}_{\mathrm{CENSO}} - G^{\mathrm{min}}_{\mathrm{CENSO}}}_{\Delta\overline{G}}, \tag{28}$$

with the gas phase electronic energy E_{gas}, a thermostatistical correction of the former based on the mRRHO model[2] $\Delta G_{\mathrm{mRRHO}}$, and the free energy of solvation ΔG_{solv}. To reduce computational cost, all three terms are only evaluated for the lowest-energy conformer. However, the Boltzmann averaged Gibbs energies are accessible at a lower level of theory ($\overline{G}_{\mathrm{CENSO}}$), which allows for an approximate inclusion of ensemble averaging by introducing a constant energy shift $\Delta\overline{G}$ with respect to the minimum free energy at lower level of theory $G^{\mathrm{min}}_{\mathrm{CENSO}}$, here after the conformational reranking with CENSO[1] (see details below). Thus, only conformational free energy contributions are neglected ($G_{\mathrm{conf}} = 0$), a justified simplification given their computational complexity and resource intensity.[3]

Generation of Docked Structures

To obtain reasonable starting structures of the non-covalently bound acid-base adducts for subsequent conformational sampling, we performed automatic (static) docking using the aISS module[4] in version 6.7.0 of the XTB program[5] at the GFN2-xTB[6]/ALPB[7] level of theory (CH_2Cl_2, $\varepsilon = 8.93$ [8]). To ensure tight convergence and to avoid potential grid complications, excessively fine settings were used for the docking (`--atm`, `--pocket`, `--opt extreme`, `--stepr 2`, `--stepa 20`, `--maxgen 15`, `--maxparent 200`, `--nstack 5000`). The docked structures of $[PdCH_2]^+$ with H_2NAr^F, H_2NAr^{Cl}, and OEt_2 were not consistent with chemical intuition, assuming a loosely bound conjugate base near the CH_2 group. Hence, an attractive potential (`scaling factor=1.0`) was added between the CH and the NH_2 group to also generate such structures.

The 15 structures lowest in energy after the final geometry optimization of each docking run were energetically reranked using part one of the CENSO routines[1], employing the efficient r^2-SCAN-3c[9] composite method with version 6.0.1 of the ORCA electronic structure program package.[10,11] Solvation effects were considered via the SMD[12] continuum model for CH_2Cl_2

and thermostatistical corrections from the single-point Hessian (SPH)[13] approach were calculated at the GFN2-xTB[6]/ALPB[7](CH_2Cl_2) level of theory. This (conformational) reranking will be referred to as CENSO reranking throughout and is the basis for determining $\Delta\overline{G}$ of a full CE for approximate ensemble averaging as used in equation (28).

The above docking and reranking procedure was iteratively applied to generate all bromonium-bridged adducts (e.g., $[HBrH{\bullet}2\,OEt_2]^+$), featuring a bromide interacting with two acid units.

Conformational Analysis

The conformational space of all investigated species was explored using the GOAT algorithm[14] (`maxitermult 6.0`, `gfnuphill gfnff`, `freezeamides true`, `autowall false`) with ORCA (refer to Section IV.I for a discussion of the chosen settings). Bond constraints were incorporated in the `%geom` block of the ORCA input for select species to preserve specific internal coordinates during conformational sampling, such as critical bonds in transition state structures or the dihedral angles for molecules presented in Figure 3c of the main manuscript. Thus, transition state structures were initially entirely optimized without addressing the conformational flexibility, followed by a comprehensive conformational analysis with essential bond constraints before reoptimizing to the final transition state structures.

All non-covalent interactions (NCI)-adducts were sampled similarly using GOAT both with and without an automatic outer wall potential (`AUTOWALL`), but also via the NCI mode with the CREST program[15–17] (version 1.2.0), again with adjusted settings (`--keepdir`, `--nci`, `--mdtemp 200`, `--wscal 0.6`, `--nmtd 6`, `--mdlen x1.5`, `--mddump 600`, `--nocross`, `--opt extreme`, `-T 24`; see Section IV.). Please note the scaled wall potential and reduced meta-dynamics (MTD) temperature, which were determined by visually checking a selection of MTD trajectories from initial test runs. A tighter wall potential is indeed crucial for any meaningful NCI sampling given that the default value only results in dissociating molecular fragments due to the applied RMSD-based bias potential. Reducing the MTD temperature also allows for more subtle NCIs to be captured as faster molecular movement at higher temperatures usually leads to immediate disruption of such low-energy NCIs.

Finally, the lowest-energy structure after full CENSO reranking of *all* obtained conformers combined from *all* conformational sampling runs was used in the subsequent geometry optimizations as detailed in the following Section. Hence, while not every specific choice of settings was rerun multiple times, a minimum combined total number of four GOAT and CREST runs effectively guarantees sufficient sampling of the NCIs (refer to Section IV. for details).

Further note that HBr dissociation was observed during the MTD runs for some of the Pd adducts with an acid, which required the introduction of bond constraints and the usage of smaller MTD time steps (`--cinp name.inp`, `--subrmsd`, `--tstep 2.5`). This was also done

for the constraints used to resolve errors in the semiempirical quantum mechanical (SQM) potential energy surface (PES) for $[HBrH{\bullet}2\,OEt_2]^+$ as described in Section IV.II.

The level of theory for the conformational benchmarking was consistently set to GFN2-xTB[6]/-ALPB[7](CH_2Cl_2) for both GOAT and CREST. However, the solvent was adjusted for the Pd(APAQ) (HFIP, $\varepsilon = 16.7$ [18,19]) and the M(OAc)(LX) (MeCN, $\varepsilon = 36.64$ [8]) systems. Since HFIP has not been parametrized for ALPB yet, benzaldehyde ($\varepsilon = 17.85$ [8]) was used instead. Hence, all CEs obtained this way were energetically reranked with CENSO as described above using the appropriate solvent for the system at hand. Additionally, test calculations also employed the GFN-FF[20] method (see Section IV.I).

Final Geometries

If not stated otherwise, all high-level DFT calculations in the following were carried out in an unrestricted fashion. The geometries obtained after conformational sampling are only of low quality and need to be reoptimized, which was done with ORCA using the efficient r^{2}SCAN-3c[9] composite method and CPCM[21,22] continuum solvation (`TIGHTOPT`, see Section III. for method justifications). Subsequent vibrational frequency analysis confirmed the nature of the stationary points on the PES (no imaginary modes: stable intermediate, exactly one imaginary mode: transition state structure) and allowed the calculation of $\Delta G_{\mathrm{mRRHO}}$. To account for isotopic substitution of hydrogen atoms with deuterium, the computed Hessian matrix was used to reevaluate the $\Delta G_{\mathrm{mRRHO}}$ contributions for every substitution pattern as detailed in Section VI.

Due to the presence of dihedral angle constraints, conventional thermostatistical corrections could not be applied to the bimetallic Pd species shown in Figure 3c, as these non-equilibrium structures violate the harmonic vibrational approximation. Instead, $\Delta G_{\mathrm{mRRHO}}$ values were obtained from SPH[13]-GFN2-xTB/ALPB calculations (`--opt extreme`), providing a more appropriate treatment of such non-stationary points on the PES.

All geometries were reoptimized in the given solvent, consequently leading to slightly altered vibrational frequency contributions for each investigated solvent. Addtionally considered solvent systems were THF ($\varepsilon = 7.52$ [8]) and DCE ($\varepsilon = 10.42$ [8]). The complete conformational workflow was not reinitiated due to the high computational cost (e.g., as for $[Pd{-}Br{-}Pd]^+$). Further, HFIP CPCM solvation was accommodated in ORCA by specifying `epsilon 16.7` in the `%cpcm` block.[18,19]

Final Electronic Energy Refinements

All electronic energies were further refined in the gas phase at the PBE0-D4[23–25]/def2-QZVPP[26,27] (def2-ECP[28] for Pd) level of theory, using tight SCF settings (`TIGHTSCF`) and large grids for nu-

merical integration (DEFGRID3). The RIJCOSX[29,30] approximation was utilized with the large def2/JK[31] auxiliary basis set. For functional benchmarking, parts of the equilibrium and thermochemical data were further evaluated using the functionals shown in Table SI15 with the def2-QZVPP basis set.

Table SI15. Functionals with corresponding references used in the functional benchmark.

Functional	References
TPSSh-D4	[24,25,32]
B3LYP-D4	[24,25,33,34]
PBE0-D4	[23–25]
r^{2}SCAN0-D4	[24,25,35]
PW6B95-D4	[24,25,36]
ωr^{2}SCAN-D4	[24,25,37]
ωB97X-V	[38,39]

Solvation Free Energies

SMD and CPCM solvation energies were computed as the energy difference of a gas- and solution-phase single point calculation with the r^{2}SCAN-3c method on the solution phase geometries, using both TIGHTSCF and DEFGRID3 in ORCA. COSMO-RS[40–42], and COSMO-RS(fine)[40–42] solvation energies were obtained with the COSMOtherm program (version C3.0, release 16.01, 2016 parameterization: BP_TZVP_C30_1601.ctd and BP_TZVPD_FINE_C30_1601.ctd, default Gsolv option). All solvation free energies are properly corrected for the change in standard state to 1 mol L^{-1}.[43]

Further Computational Details

Identical activity and diffusion coefficients for all pairs of oxidized and reduced species were assumed to approximate the experimentally measured half-potentials with herein computed redox potentials.[44] Using the direct approach[45,46], all potentials are reported against the Fc/Fc$^+$ redox couple *calculated* in eclipsed conformation[47] with THF as the solvent.

The free energy of $H^+_{(solv)}$ cannot be calculated by quantum chemical methods[48] and is thus prone to errors, which is why an isodesmic scheme[49] was constructed with 2,4,6-trimethylpyridinium (pK_a^{THF} = 8.1 [50]) as an experimental reference point for computing the pK_a values in THF solvent. Similarly, BDFEs can be calculated using an isodesmic approach[51], which in this work was anchored to the experimental BDFE of TEMPOH (BDFE(THF) = 65.5 kcal mol^{-1} [52]).

ChimeraX[53,54] (version 1.9) was used for visualization purposes.

III. Method Assessment for Obtaining Molecular Geometries

Table SI16. Comparison of key bond lengths of $[PdCH_2]^+$ (in Å) for different methods versus the experimental crystal structure (XRD). PBE0-D4, and TPSSh-D4 were employed with the def2-TZVP basis set, and CPCM(CH_2Cl_2) was used throughout. The RMSD and its heavy variant without consideration of hydrogen atoms (hRMSD) are given w.r.t the XRD structure (in Å). The XRD was used as an initial guess structure to ensure comparability.

Bond	XRD	r^{2}SCAN-3c	ωB97X-3c[55]	PBE0-D4	TPSSh-D4
Pd1–Br1	2.41	2.45	2.44	2.42	2.43
Pd1–P1	2.33	2.35	2.35	2.33	2.33
Pd1–P2	2.32	2.36	2.35	2.33	2.34
Pd1–C47	2.30	2.31	2.29	2.27	2.28
Pd1–H47A	2.25	2.29	2.23	2.21	2.21
Pd1–H47B	1.67	1.71	1.73	1.71	1.72
C47–H47A	0.87	1.10	1.10	1.10	1.10
C47–H47B	0.87	1.18	1.15	1.17	1.17
RMSD	-	0.50	0.53	0.57	0.57
hRMSD	-	0.33	0.37	0.40	0.40

Table SI17. Comparison of key bond lengths (in Å) for the symmetric transition state structures of $[PdCH_2]^+$ optimized with different computational methods. PBE0-D4, and TPSSh-D4 were employed with the def2-TZVP basis set, and CPCM(CH_2Cl_2) was used throughout.

Bond	r^{2}SCAN-3c	ωB97X-3c[55]	PBE0-D4	TPSSh-D4
Pd1–Br1	2.44	2.44	2.42	2.43
Pd1–P1	2.34	2.34	2.32	2.33
Pd1–P2	2.34	2.34	2.32	2.33
Pd1–C47	2.27	2.26	2.24	2.25
Pd1–H47A	1.94	1.93	1.92	1.93
Pd1–H47B	1.95	1.95	1.92	1.92

Tables SI16 and SI17 contain key bond lengths of the asymmetric $[PdCH_2]^+$ and its symmetric transition state as calculated with different methods.

As expected, the XRD reference structure is sufficiently reproduced by all methods, and the deviations to the experimental structure are consistent between the composite methods and

the employed hybrid density functional approximations (DFAs). A similar picture emerges for the transition state structures, for which only minimal deviations between methods can be observed, suggesting that r^{2}SCAN-3c is suitable for computing both minimum structures and barrier heights in this study (e.g., despite lacking exact exchange[56]). Systematic discrepancies, such as those in the Pd1–H47A/B bond lengths, likely stem from solid-state packing effects that cannot be captured by single molecule solution phase calculations, regardless of the chosen DFT method.

IV. Tackling the Conformational Challenge

IV.I Initial Tests for [Pd−Br−Pd]$^+$

Exploring the conformational space of flexible molecules becomes increasingly challenging as molecular size increases. To address this challenge, we evaluated two state-of-the-art approaches for conformational sampling (GOAT[14], CREST[16]) with varying settings and SQM methods for the conformationally most challenging system in our study, the bimetallic Pd complex ([Pd−Br−Pd]$^+$). Table SI18 provides the relative Gibbs energies of the lowest-energy conformer after full CENSO reranking as obtained from a specific run, where the following changes to default settings may apply:

CREST:

- GFN-FF: MTD simulations were carried out with the efficient GFN-FF force field with ALPB solvation, and the geometries of the resulting CE were subsequently relaxed at GFN2-xTB/ALPB level of theory.
- LONGMTD: The MTD simulation length was increased to 250 ps or 500 ps for GFN2-xTB or GFN-FF runs, respectively. For reference, CREST otherwise uses a value of approximately 100 ps for this specific system.

GOAT:

- GFNUPHILL: Use GFN-FF for the uphill steps, reducing the computational cost of each GOAT iteration.
- MAXITERMULT: Change the multiplication factor for the number of geometry optimizations per worker from the default value of 3 to 6, which increases the length of each GOAT iteration, similar to increasing the MTD time length, albeit at a different scale.
- OPTTIGHT: Also set the optimization threshold for GOAT runs to `OPTTIGHT` in ORCA.

Table SI18. Relative Gibbs energies of each lowest-energy conformer as obtained from different CREST and GOAT runs after full CENSO reranking.

Run Mode	G_{rel} (kcal/mol)
GOAT + GFNUPHILL + MAXITERMULT	0.000
GOAT + OPTTIGHT	0.236
GOAT + GFNUPHILL	0.248
GOAT (default)	0.249
CREST + GFN2-xTB + LONGMTD	0.185
CREST + GFN2-xTB (default)	0.645
CREST + GFN2-xTB (default, second run)	0.845
CREST + GFN-FF (default)	3.987
CREST + GFN-FF + LONGMTD	5.059

Please note that for an appropriate comparison of CREST with GOAT, a minimum of at least three or ideally even more runs would be needed for each specific change in settings due to the non-deterministic nature of both approaches, prohibiting a direct comparison of individual runs.

Nevertheless, the energetic ranking in Table SI18 is still insightful, indicating GOAT to be more robust in finding a minimum energy structure for this molecular example. Both approaches are sensitive to the effective simulation time lengths (`LONGMTD` and `MAXITERMULT`), where larger values are beneficial. Hence, after visual inspection of multiple MTD runs in the NCI CREST mode as used for the acid-base complexes (see Section II.), the MTD time lengths were scaled to 150 %.

Additionally, as is somewhat expected, relaxing the geometries of a GFN-FF-CE with GFN2-xTB does not necessarily redeem the quality of a full conformational exploration with GFN2-xTB. Finally, using the `GFNUPHILL` keyword approximately reduces the overall computation time by a factor of two, while seemingly retaining the robustness of a regular GOAT run.

Based on these results, it appears most promising to employ the GOAT algorithm in combination with both `GFNUPHILL` and `MAXITERMULT` for conformational analysis, where `GFNUPHILL` nicely compensates the greater computational cost of increasing `MAXITERMULT`.

IV.II Addressing Errors in the Semiempirical Potential Energy Surface of $[HBrH{\bullet}2\,OEt_2]^+$

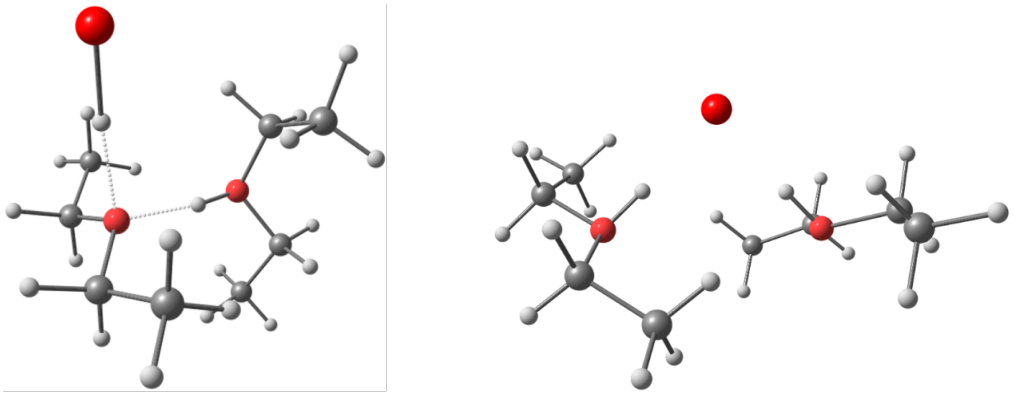

(a) (b)

Figure SI56. Lowest structure for $[HBrH{\bullet}2\,OEt_2]^+$ after CENSO reranking as obtained from the best GOAT run (GFN2-xTB geometry) (a), and the overall lowest structure (r^2SCAN-3c) found as described in the text below (b).

Initially, the different NCI runs (CREST, GOAT with/without `AUTOWALL`, etc.) were compared after full CENSO reranking using the GFN2-xTB optimized geometries. However, preliminary tests with r^2SCAN-3c revealed that there is a significant error in the PES of GFN2-xTB for $[HBrH{\bullet}2\,OEt_2]^+$ as exemplified by the two structures in Figure SI56. The structure resulting from the best GOAT run (Figure SI56a) is an adduct of HBr with the cation of Brookhart's acid instead of the bromonium bridged species as proposed in the main text (Figure SI56b). At GFN2-xTB/ALPB, the latter is 5.1 kcal mol^{-1} higher in energy, whereas the qualitative ranking is completely reversed at r^2SCAN-3c/SMD level of theory, at which the former is 9.8 kcal mol^{-1} higher in energy. Hence, one can expect significant issues with the conformational sampling given that all intermediate structures are necessarily ranked at the GFN2-xTB/ALPB level of theory, motivating us to conduct a more thorough analysis to obtain the actual minimum structure of $[HBrH{\bullet}2\,OEt_2]^+$.

For this, we performed multiple CREST runs, symmetrically constraining both H−Br hydrogen bonds systematically from 1.30 Å to 2.5 Å with a step size of 0.05 Å. All resulting CEs were subsequently reranked with CENSO, the lowest-energy structure optimized with r^2SCAN-3c/CPCM and finally reranked at PBE0-D4/def2-QZVPP/SMD + $\Delta G_{\mathrm{mRRHO}}$(GFN2-xTBALPB-SPH) level of theory. Hence, we effectively utilized a multitude of reasonable initial guess geometries for the r^2SCAN-3c optimizations, finally resulting in a geometry that is mostly free of the GFN2-xTB error and indeed the lowest-energy structure obtained for $[HBrH{\bullet}2\,OEt_2]^+$ within this study.

Relevant in this context, g-xTB is a novel SQM method currently developed by the Grimme

group that substantially enhances the accuracy of GFN2-xTB with only marginal additional computational cost. It will be detailed in a forthcoming publication. Notably, a preliminary version of g-xTB accurately predicts the energy ordering of the $[HBrH{\bullet}2\,OEt_2]^+$ structures, showing remarkable concordance with the higher-level DFT methods employed herein. Consequently, the parallelity of the g-xTB PES relative to more sophisticated DFT methods can be leveraged in future conformational exploration, thus avoiding errors such as those described in this Section.

V. Assessing the Performance of Various Density Functional Approximations and Implicit Solvation Models

Table SI19. Statistical measures for the five best-performing combinations of method and solvation model on the equilibrium data studied herein, with all energies given in units of kcal mol^{-1}.

Solvation Model	Method	ME	MAE	AMAX	MAX	MIN	SD	N
COSMO-RS(fine)	r^{2}SCAN0-D4	-1.06	1.77	2.96	1.12	-2.96	1.72	8
SMD	PBE0-D4	-1.75	2.35	4.17	1.46	-4.17	2.26	8
SMD	ωr^{2}SCAN-D4	-2.22	2.45	4.43	0.95	-4.43	1.95	8
SMD	TPSSh-D4	-1.65	2.50	4.31	2.30	-4.31	2.47	8
COSMO-RS(fine)	PW6B95-D4	-2.26	2.62	4.23	0.95	-4.23	2.19	8

Table SI20. Comparison of the five best-performing method and solvation model combinations for the equilibrium data here listed with the predicted redox potentials for $[PdCH_2]^+$, with all values given in units of V. ΔE_0 corresponds to the deviation from the experimental value.

Solvation Model	Method	E_0^{calc}(Ni)	E_0^{calc}(Pd)	ΔE_0(Ni)	ΔE_0(Pd)[a]
COSMO-RS(fine)	r^{2}SCAN0-D4	0.281	1.020	0.126	0.214
SMD	PBE0-D4	0.046	0.590	-0.109	-0.220
SMD	ωr^{2}SCAN-D4	0.117	0.558	-0.038	-0.252
SMD	TPSSh-D4	-0.030	0.358	-0.185	-0.452
COSMO-RS(fine)	PW6B95-D4	0.322	0.770	0.167	-0.040

[a] Irreversible oxidation; difference calculated to anodic peak potential.

Table SI21. Comparison of the five best-performing method and solvation model combinations for the equilibrium data here listed with the predicted BDFEs for $[PdCH_2]^+$, with all values given in units of kcal mol^{-1}. ΔBDFE corresponds to the deviation from the experimental value.

Solvation Model	Method	BDFE^{calc}(Ni)	BDFE^{calc}(Pd)	ΔBDFE(Ni)	ΔBDFE(Pd)[a]
COSMO-RS(fine)	r^{2}SCAN0-D4	63.3	71.5	-6.7	-5.4
SMD	PBE0-D4	71.1	74.3	1.1	-2.6
SMD	ωr^{2}SCAN-D4	75.8	77.0	5.8	0.1
SMD	TPSSh-D4	71.8	72.2	1.8	-4.7
COSMO-RS(fine)	PW6B95-D4	65.9	68.1	-4.1	-8.8

[a] Experimental BDFE was calculated using the experimental pKa *and* the computed E_0 data.

Table SI22. Comparison of the five best-performing method and solvation model combinations for the equilibrium data here listed with the predicted pKa for $[PdCH_2]^+$. ΔpKa corresponds to the deviation from the experimental value and ΔΔpKa(Ni-Pd) is the computed acidification upon substituting Ni with Pd.

Solvation Model	Method	pKa^{calc}(Ni)	pKa^{calc}(Pd)	ΔpKa(Ni)	ΔpKa(Pd)	ΔΔpKa(Ni-Pd)
COSMO-RS(fine)	r^{2}SCAN0-D4	-3.7	-10.3	-7.9	-8.7	6.6
SMD	PBE0-D4	3.0	-3.9	-1.2	-2.3	6.9
SMD	ωr^{2}SCAN-D4	2.2	-4.3	-2.0	-2.7	6.5
SMD	TPSSh-D4	2.8	-3.4	-1.4	-1.8	6.2
COSMO-RS(fine)	PW6B95-D4	-4.8	-10.8	-9.0	-9.2	6.0

Table SI19 provides statistical measures on the performance of the five best combinations of implicit solvation model and DFA, with r^{2}SCAN0-D4/COSMO-RS(fine) to yield the lowest MAE on the experimentally accessible equilibrium data in THF and DCE ($N = 5 + 3 = 8$, excluding the deuterated equilibrium K_1). However, Tables SI21 and SI22 clearly show that this level of theory does not perform equally well in predicting the thermochemical data of $[PdCH_2]^+$ (e.g., significant deviation from experimental BDFEs and pKas). Further, it is well known that pKa values computed with COSMO-RS(fine) solvation need to be corrected via linear free energy relationships due to systematic deviations compared to experiment.[57]

Thus, to circumvent any empirical corrections to the pKas or BDFEs, we chose to employ the second-best performing method and solvation model combination, namely PBE0-D4 with SMD solvation, providing the best compromise between accurate equilibrium and $[PdCH_2]^+$ property data. PBE0 is a generally robust hybrid DFA with only one empirical parameter, known for excellent performance also on electronically complicated metal species.[58,59] Additionally, due to favorable error cancellation, the key shift in predicted acidification upon going from the nickel to the palladium species as one of the key results of this study is consistently reproduced for all employed levels of theory (± 1 pKa unit error), further supporting the roughly

millionfold increase in C-H bond acidity (~6 pKa units) as observed experimentally. Please note that the data for all remaining method combinations not shown above can be found as `.csv` files in the appended `.zip` folder.

VI. Modeling Isotopic Substitution in the Dynamic K_1 Equilibrium

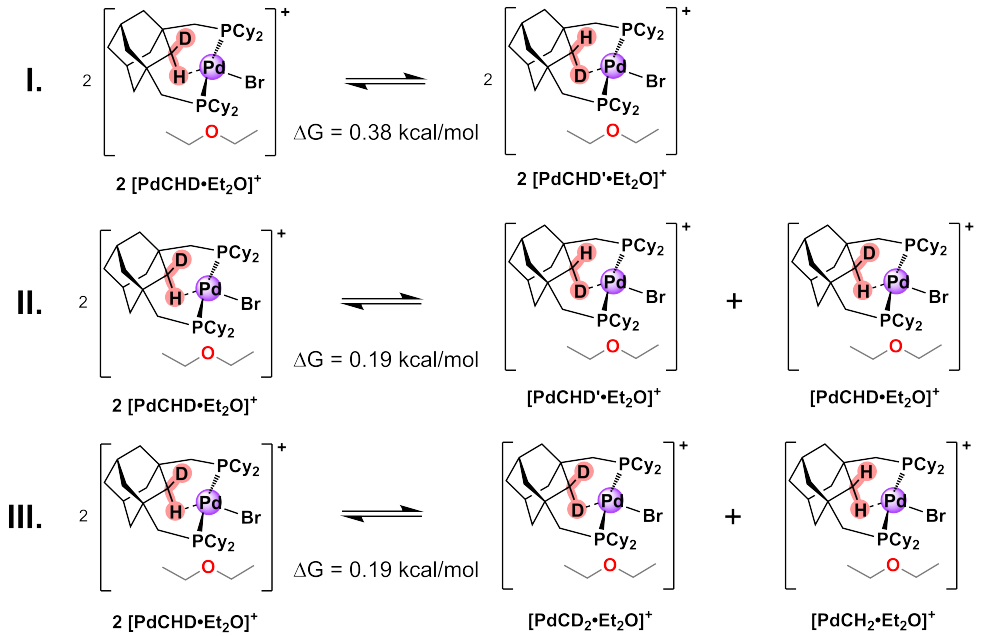

Figure SI57. Gibbs free energitcs for the isotopic substitution of two equivalents of $[PdCH_2{\bullet}Et_2O]^+$.

Figure 4a of the main text shows all six protons of the K_1 equilibrium that undergo slow exchange in solution. Isotopic substitution of two of these protons, based on the stoichiometry of the reaction with deuterated acid, generates numerous possible substitution patterns and thus structure combinations, all contributing to the experimentally observed equilibrium isotope effect (EIE). To investigate this computationally, we first determined the distribution of two deuterium on the reagent side of the equilibrium (see Figure SI57), revealing that substitution of H47A with longer distance to palladium (and thus higher stretching frequency) is energetically favored, which has been reported for an agostic osmium complex before.[60]

Assuming the lowest-energy structure with both deuterium residing in the H47A position to be most populated, the isotopic shift of the K_1 equilibrium can be approximated by thermostatistically averaging over all six possible reactions starting from two equivalents of $[PdCHD{\bullet}Et_2O]^+$ as shown in Figure SI58. This analysis finally yields an equilibrium free energy of 1.08 kcal mol^{-1} for the deuterated K_1 equilbrium in CH_2Cl_2, including an isotopic shift of

0.22 kcal mol^{-1}, which corresponds to a computational EIE of 1.5. Both the isotopic shift and EIE values remain consistent when calculated at 298 K and 283 K, with precision to two and one significant digits, respectively.

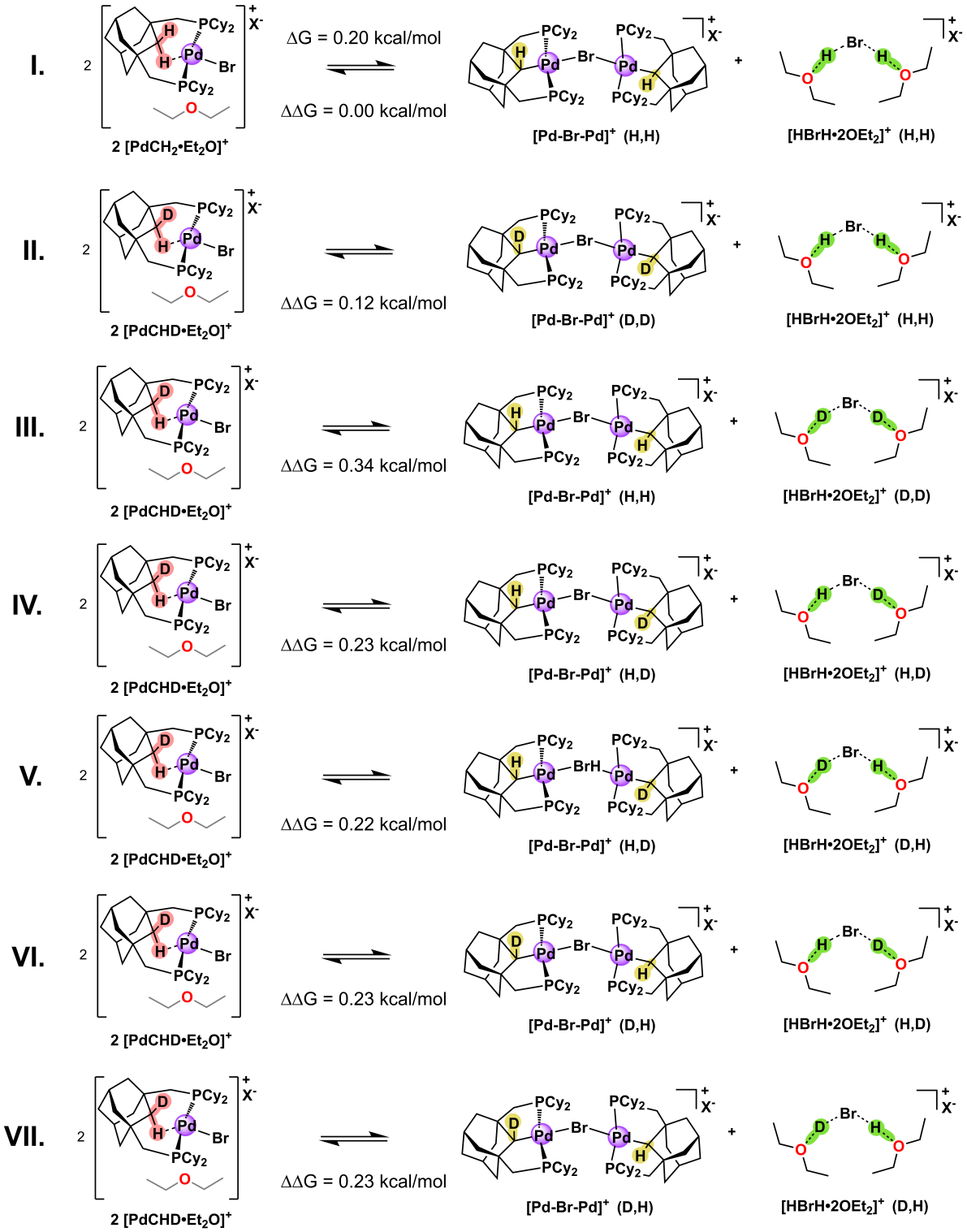

Figure SI58. Shift in Gibbs free energy ($\Delta\Delta G$) upon substituting two of the exchanging protons (marked in red, green and yellow, respectively) with deuterium for all six combinations relative to the undeuterated equilibrium with experimental reaction energy of $\Delta G = 0.20\,\mathrm{kcal\,mol^{-1}}$.

VII. List of Abbreviations

aISS	automated interaction site screening
ALPB	analytical linearized Poisson-Boltzmann
AMAX	absolute maximal error
APAQ	acetyl-protected aminoquinoline
BDFE	bond dissociation free energy
CE	conformer ensemble
CENSO	command-line energetic sorting
COSMO-RS	conductor like screening model for real solvents
CPCM	conductor-like polarizable continuum model
CREST	conformer–rotamer ensemble sampling tool
DCE	1,2-dichloroethane
DFA	density functional approximation
DFT	density functional theory
EIE	equilibrium isotope effect
Fc^+/Fc	ferrocenium/ferrocene redox-couple
GFN	geometries, vibrational frequencies and noncovalent interactions
GOAT	global optimization algorithm
HFIP	1,1,1,3,3,3–hexafluoro–2–propanol
MAE	mean absolute error
MAX	maximal error
Me	methyl
ME	mean error
MeCN	acetonitrile
MIN	minimal error
mRRHO	modified rigid-rotor harmonic-oscillator
MTD	meta-dynamics
NCI	non-covalent interactions
PES	potential energy surface
RMSD	root-mean-square deviation
SCF	self-consistent field
SD	standard deviation
SMD	solvation model based on the solute electron density
SPH	single-point Hessian
SQM	semiempirical quantum mechanical
TEMPOH	1-hydroxy-2,2,6,6-tetramethylpiperidine
THF	tetrahydrofuran

TS	transition state
XRD	X-ray diffraction
xTB	extended tight-binding

XIX. References

[1] S. Grimme, F. Bohle, A. Hansen, P. Pracht, S. Spicher, M. Stahn, *J. Phys. Chem. A* **2021**, *125*, 4039–4054.

[2] S. Grimme, *Chem. Eur. J.* **2012**, *18*, 9955–9964.

[3] P. Pracht, S. Grimme, *Chem. Sci.* **2021**, *12*, 6551–6568.

[4] C. Plett, S. Grimme, *Angew. Chem. Int. Ed.* **2023**, *62*, e202214477.

[5] C. Bannwarth, E. Caldeweyher, S. Ehlert, A. Hansen, P. Pracht, J. Seibert, S. Spicher, S. Grimme, *WIREs Comput Mol Sci.* **2021**, *11*, e1493.

[6] C. Bannwarth, S. Ehlert, S. Grimme, *J. Chem. Theory Comput.* **2019**, *15*, 1652–1671.

[7] S. Ehlert, M. Stahn, S. Spicher, S. Grimme, *J. Chem. Theory Comput.* **2021**, *17*, 4250–4261.

[8] D. R. Lide, C. R. Company (Eds.), *CRC Handbook of Chemistry and Physics 90th ed.*, CRC Press, Boca Raton, FL, **2009**.

[9] S. Grimme, A. Hansen, S. Ehlert, J.-M. Mewes, *J. Chem. Phys.* **2021**, *154*, 064103.

[10] F. Neese, *WIREs Comput Mol Sci.* **2022**, *12*, e1606.

[11] F. Neese, *J. Comput. Chem.* **2023**, *44*, 381–396.

[12] A. V. Marenich, C. J. Cramer, D. G. Truhlar, *J. Phys. Chem. B* **2009**, *113*, 6378–6396.

[13] S. Spicher, S. Grimme, *J. Chem. Theory Comput.* **2021**, *17*, 1701–1714.

[14] B. De Souza, *Angew. Chem. Int. Ed.* **2025**, e202500393.

[15] S. Grimme, *J. Chem. Theory Comput.* **2019**, *15*, 2847–2862.

[16] P. Pracht, F. Bohle, S. Grimme, *Phys. Chem. Chem. Phys.* **2020**, *22*, 7169–7192.

[17] P. Pracht, S. Grimme, C. Bannwarth, F. Bohle, S. Ehlert, G. Feldmann, J. Gorges, M. Müller, T. Neudecker, C. Plett, S. Spicher, P. Steinbach, P. A. Wesołowski, F. Zeller, *J. Chem. Phys.* **2024**, *160*, 114110.

[18] J. M. Ramos-Villaseñor, E. Rodríguez-Cárdenas, C. E. Barrera Díaz, B. A. Frontana-Uribe, *J. Electrochem. Soc.* **2020**, *167*, 155509.

[19] Y.-F. Yang, G. Chen, X. Hong, J.-Q. Yu, K. N. Houk, *J. Am. Chem. Soc.* **2017**, *139*, 8514–8521.

[20] S. Spicher, S. Grimme, *Angew. Chem. Int. Ed.* **2020**, *59*, 15665.

[21] V. Barone, M. Cossi, *J. Phys. Chem. A* **1998**, *102*, 1995–2001.

[22] M. Cossi, N. Rega, G. Scalmani, V. Barone, *J. Comput. Chem.* **2003**, *24*, 669.

[23] C. Adamo, V. Barone, *J. Chem. Phys.* **1999**, *110*, 6158–6170, pbe0.

[24] E. Caldeweyher, C. Bannwarth, S. Grimme, *J. Chem. Phys.* **2017**, *147*, 034112.

[25] E. Caldeweyher, S. Ehlert, A. Hansen, H. Neugebauer, S. Spicher, C. Bannwarth, S. Grimme, *J. Chem. Phys.* **2019**, *150*, 154122, d4.

[26] F. Weigend, F. Furche, R. Ahlrichs, *J. Chem. Phys.* **2003**, *119*, 12753–12762.

[27] F. Weigend, R. Ahlrichs, *Phys. Chem. Chem. Phys.* **2005**, *7*, 3297–3305.

[28] D. Andrae, U. Häußermann, M. Dolg, H. Stoll, H. Preuß, *Theoret. Chim. Acta* **1990**, *77*, 123–141.

[29] F. Neese, F. Wennmohs, A. Hansen, U. Becker, *Chem. Phys.* **2009**, *356*, 98–109.

[30] B. Helmich-Paris, B. De Souza, F. Neese, R. Izsák, *J. Chem. Phys.* **2021**, *155*, 104109.

[31] F. Weigend, *J. Comput. Chem.* **2008**, *29*, 167–175.

[32] V. N. Staroverov, G. E. Scuseria, J. Tao, J. P. Perdew, *J. Chem. Phys.* **2003**, *119*, 12129–12137, tpssh.

[33] C. Lee, W. Yang, R. G. Parr, *Phys. Rev. B* **1988**, *37*, 785.

[34] A. D. Becke, *Phys. Rev. A* **1988**, *38*, 3098.

[35] M. Bursch, H. Neugebauer, S. Ehlert, S. Grimme, *J. Chem. Phys.* **2022**, *156*, 134105.

[36] Y. Zhao, D. G. Truhlar, *J. Phys. Chem. A* **2005**, *109*, 5656–5667.

[37] L. Wittmann, H. Neugebauer, S. Grimme, M. Bursch, *J. Chem. Phys.* **2023**, *159*, 224103.

[38] N. Mardirossian, M. Head-Gordon, *Phys. Chem. Chem. Phys.* **2014**, *16*, 9904–9924.

[39] O. A. Vydrov, T. Van Voorhis, *J. Chem. Phys.* **2010**, *133*, 244103.

[40] A. Klamt, *J. Phys. Chem.* **1995**, *99*, 2224–2235.

[41] A. Klamt, V. Jonas, T. Bürger, J. C. W. Lohrenz, *J. Phys. Chem. A* **1998**, *102*, 5074–5085.

[42] A. Klamt, *WIREs Comput Mol Sci.* **2011**, *1*, 699–709.

[43] C. J. Cramer, *Essentials of Computational Chemistry: Theories and Models 2nd ed.*, Wiley, Chichester, West Sussex, England; Hoboken, NJ, **2004**.

[44] O. Hammerich, B. Speiser (Eds.), *Organic Electrochemistry: Revised and Expanded 5th ed.*, CRC Press, Boca Raton, FL, **2015**.

[45] J. Ho, *Phys. Chem. Chem. Phys.* **2015**, *17*, 2859–2868.

[46] J. Ho, M. Z. Ertem, *J. Phys. Chem. B* **2016**, *120*, 1319–1329.

[47] F. Wang, N. Mohammadi, S. P. Best, D. Appadoo, C. T. Chantler, *Radiat. Phys. Chem.* **2021**, *188*, 109590.

[48] K. S. Alongi, G. C. Shields in *Annual Reports in Computational Chemistry*, *Vol. 6*, Elsevier, **2010**, pp. 113–138.

[49] S. Sastre, R. Casasnovas, F. Muñoz, J. Frau, *Phys. Chem. Chem. Phys.* **2016**, *18*, 11202–11212.

[50] T. Rodima, I. Kaljurand, A. Pihl, V. Mäemets, I. Leito, I. A. Koppel, *J. Org. Chem.* **2002**, *67*, 1873–1881.

[51] W. Treyde, K. Riedmiller, F. Gräter, *RSC Adv.* **2022**, *12*, 34557–34564.

[52] C. F. Wise, R. G. Agarwal, J. M. Mayer, *J. Am. Chem. Soc.* **2020**, *142*, 10681–10691.

[53] E. F. Pettersen, T. D. Goddard, C. C. Huang, G. S. Couch, D. M. Greenblatt, E. C. Meng, T. E. Ferrin, *J. Comput. Chem.* **2004**, *25*, 1605–1612.

[54] E. F. Pettersen, T. D. Goddard, C. C. Huang, E. C. Meng, G. S. Couch, T. I. Croll, J. H. Morris, T. E. Ferrin, *Protein Sci.* **2021**, *30*, 70–82.

[55] M. Müller, A. Hansen, S. Grimme, *J. Chem. Phys.* **2023**, *158*, 014103.

[56] K. R. Bryenton, A. A. Adeleke, S. G. Dale, E. R. Johnson, *WIREs Comput Mol Sci.* **2023**, *13*.

[57] A. Klamt, F. Eckert, M. Diedenhofen, M. E. Beck, *J. Phys. Chem. A* **2003**, *107*, 9380–9386.

[58] S. Dohm, A. Hansen, M. Steinmetz, S. Grimme, M. P. Checinski, *J. Chem. Theory Comput.* **2018**, *14*, 2596–2608.

[59] L. R. Maurer, M. Bursch, S. Grimme, A. Hansen, *J. Chem. Theory Comput.* **2021**, *17*, 6134–6151.

[60] R. B. Calvert, J. R. Shapley, *J. Am. Chem. Soc.* **1978**, *100*, 7726–7727.